LETTER

Robust wireless power transfer using a nonlinear parity–time–symmetric circuit

Sid Assawaworrarit[1], Xiaofang Yu[1] & Shanhui Fan[1]

Considerable progress in wireless power transfer has been made in the realm of non-radiative transfer, which employs magnetic-field coupling in the near field[1–4]. A combination of circuit resonance and impedance transformation is often used to help to achieve efficient transfer of power over a predetermined distance of about the size of the resonators[3,4]. The development of non-radiative wireless power transfer has paved the way towards real-world applications such as wireless powering of implantable medical devices and wireless charging of stationary electric vehicles[1,2,5–8]. However, it remains a fundamental challenge to create a wireless power transfer system in which the transfer efficiency is robust against the variation of operating conditions. Here we propose theoretically and demonstrate experimentally that a parity–time-symmetric circuit incorporating a nonlinear gain saturation element provides robust wireless power transfer. Our results show that the transfer efficiency remains near unity over a distance variation of approximately one metre, without the need for any tuning. This is in contrast with conventional methods where high transfer efficiency can only be maintained by constantly tuning the frequency or the internal coupling parameters as the transfer distance or the relative orientation of the source and receiver units is varied. The use of a nonlinear parity–time-symmetric circuit should enable robust wireless power transfer to moving devices or vehicles[9,10].

The idea of wireless power transfer has a long history of development dating back to Tesla's vision of long-distance wireless electrical power transmission[11]. Early applications used a focused, narrow microwave beam that led to an efficient, long-range, point-to-point power transfer but required strenuous tracking as a consequence of beam directionality[12]. Recently, non-radiative wireless power transfer using magnetic resonance coupling in the near field as a power transfer mechanism has been extensively developed[1–4]. This type of wireless power transfer is often tuned to work efficiently at a specific transfer distance and, consequently, is not robust against variations in operating conditions[4]. For the often used wireless power transfer scheme shown in Fig. 1a, either the in- and out-coupling strength (γ_1, γ_2) or the operating frequency ω of the source must be adjusted as the transfer distance varies, in order to maintain optimal efficiency[3,13].

The invention of a robust wireless power transfer system that eliminates the need for active tuning while maintaining high efficiency could widen the application area of wireless power transfer technology to include dynamic charging, such as delivering power wirelessly to travelling vehicles[9]. Here, we propose a parity–time (PT)-symmetric circuit that incorporates a nonlinear saturable gain element into the source that serves as a time-reversed counterpart to the device's dissipation (Fig. 1b). We propose theoretically and demonstrate experimentally that the physics of PT symmetry combined with nonlinear saturation self-selects the operating frequency that corresponds to the maximum efficiency and hence guarantees optimal power transfer over a wide range of transfer distances, all without the need for any active tunings required by the conventional scheme (Fig. 1c).

PT-symmetric systems are invariant under the joint parity and time reversal operation[14,15]. In optical systems, where the symmetry conditions can be met by engineering the gain/loss regions and their coupling, PT-symmetric systems have exhibited unusual properties[16–20]. A linear PT-symmetric system supports two phases, depending on the magnitude of the gain/loss relative to the coupling strength. In the unbroken or exact phase, eigenmode frequencies remain real and energy is equally distributed between the gain and loss regions; in the broken phase, one of the eigenmodes grows exponentially while the other decays exponentially. Recently, the concept of PT symmetry has been extensively explored in laser structures[21–24]. Theoretically, the inclusion of nonlinear gain saturation in the analysis of a PT-symmetric system causes that system to reach a steady state in a laser-like fashion that still contains the following PT symmetry characteristics[25,26]: the selection of the lasing frequency based on that of the PT eigenmode and the control of the steady-state intensities by the gain saturation mechanism. Complementing these works, here we explore the consequence of PT symmetry with nonlinear gain saturation in wireless power transfer systems.

To describe how PT symmetry leads to a robust wireless power transfer scheme, we present an analysis based on a coupled-mode theory[27] model of a two-resonance system consisting of a source resonator coupled to a receiver resonator, as shown in Fig. 2a. The source resonator has a resonant frequency ω_1, a gain rate g_{10}, and an intrinsic loss rate γ_{10} giving an overall gain rate of $g_1 = g_{10} - \gamma_{10}$. The receiver resonator has a resonant frequency $\omega_2 \approx \omega_1$ and a loss rate $\gamma_2 = \gamma_1 + \gamma_{20}$, where γ_1 is the loss rate contributed by the receiver's load and γ_{20} is the intrinsic loss rate of the receiver. The two resonators are coupled together with a coupling rate κ, which in a wireless power transfer system is a function of the source-to-receiver separation distance. Power is fed into the source via its gain element before being transferred through coupling to the receiver. The system dynamics are described by:

$$\frac{d}{dt}\begin{bmatrix} a_1 \\ a_2 \end{bmatrix} = \begin{bmatrix} i\omega_1 + g_1 & -i\kappa \\ -i\kappa & i\omega_2 - \gamma_2 \end{bmatrix}\begin{bmatrix} a_1 \\ a_2 \end{bmatrix} \tag{1}$$

where the subscript 1 (or 2) refers to the source (or receiver) and $a_{1,2}$ are the field amplitudes defined such that $|a_{1,2}|^2$ represent the energies stored in each object. To find the eigenfrequencies, we let $a_{1,2} \propto e^{i\omega t}$ and obtain the characteristic equation:

$$(i(\omega_1 - \omega) + g_1)(i(\omega_2 - \omega) - \gamma_2) + \kappa^2 = 0 \tag{2}$$

Unlike the usual approach used for the study of linear PT-symmetric system, in which one imposes an externally fixed value of gain g_1 and computes the eigenfrequency, which in general is complex, here we consider a PT-symmetric system with a nonlinear saturable gain; that is, we assume that g_1 depends on the energy stored in the source resonator $|a_1|^2$. We will see that for steady-state dynamics the detail of this dependency is not important. In this case, in analogy with laser

[1]Department of Electrical Engineering, Ginzton Laboratory, Stanford University, Stanford, California 94305, USA.
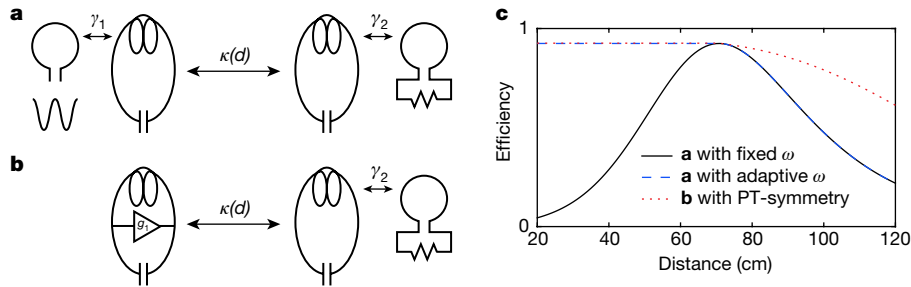
Figure 1 | Comparison between conventional and PT-symmetry-based wireless power transfer schemes as the source–receiver resonant coupling rate κ varies as a function of transfer distance d.
a, Conventional scheme. A harmonic wave at a frequency ω is generated, coupled to the source resonator at a rate γ_1, transferred across distance d before being delivered to the load at the receiver resonator at a rate γ_2. **b**, PT-symmetric scheme. Power is generated at the source resonator via a gain element with a gain rate g_1, transferred to and taken out at the receiver resonator by a load with a loss rate γ_2. **c**, Transfer efficiency as a function of the separation distance between source and receiver for a conventional scheme without frequency tuning (black line), a conventional scheme with adaptive frequency tuning (blue dashed line) and a PT-symmetry-based scheme (red dotted line).

theory[28], we search for a steady-state solution of equation (2) with a real ω while allowing g_1 to vary. The strength of g_1 corresponding to such a steady-state solution then defines the saturated gain level $g_{1,\text{sat}}$. Taking ω to be real, we separate the real and imaginary parts of equation (2) to obtain:

$$(\omega - \omega_1)(\omega - \omega_2)^2 + \gamma_2^2(\omega - \omega_1) - \kappa^2(\omega - \omega_2) = 0 \tag{3}$$

$$g_{1,\text{sat}} = \gamma_2 \frac{\omega - \omega_1}{\omega - \omega_2} \tag{4}$$

where equation (3) gives the eigenfrequencies ω for a given loss rate γ_2 and coupling rate κ. Equation (4) then provides the corresponding saturated gain value at which the system oscillates as a steady state with frequency ω. Additionally, despite the possibility of having multiple solutions for the steady-state mode frequencies, for the simple gain model, the mode requiring the lowest gain will grow to reach its steady state and saturate out the gain, preventing other modes from accessing the gain level they need to reach steady-state oscillation. Further analyses reveal this steady-state solution to be stable (Extended Data Fig. 1). Also, in the presence of a sudden change in the coupling rate, the system settles into a steady state within a few cycles (Extended Data Fig. 2).

In the case of a matched resonance ($\omega_1 = \omega_2 = \omega_0$), there are two regions containing solutions of equations (3) and (4), depending on the relative values of κ and γ_2, as shown in Fig. 2b. In the strong coupling region ($\kappa \geq \gamma_2$), the system support two modes with frequencies $\omega = \omega_0 \pm \sqrt{\kappa^2 - \gamma_2^2}$, and these two modes have the same saturated gain, exactly balancing out the loss, that is, $g_{1,\text{sat}} = \gamma_2$. In addition, these two modes have equal amplitude distribution, that is, $|a_2/a_1| = 1$. Therefore, these modes satisfy an exact PT symmetry. Unlike the linear PT system, where the PT symmetry of the eigenmodes in the exact phase is enforced by choosing a system Hamiltonian that is PT-symmetric, here the PT symmetry of the eigenmodes emerges from the nonlinear dynamics of gain saturation: at steady state, the mode of the system automatically has PT symmetry. We note that although $\omega = \omega_0$ is also a solution of equation (3) in the strong coupling region, this mode requires higher saturated gain as κ increases and is thus not shown in Fig. 2b. In the weak coupling region ($\kappa < \gamma_2$), only one real mode is located at $\omega = \omega_0$, with the corresponding saturated gain $g_{1,\text{sat}} = \kappa^2/\gamma_2 < \gamma_2$. Similar to the linear PT system, here we observe a bifurcation in the real part of the modal frequency at $\kappa = \gamma_2$. Unlike the linear PT system, however, the imaginary part of the modal frequency in our system remains zero in both regions. We note that our results agree with those of refs 25 and 26 without making any assumption a priori on the gain saturation mechanism, which influences only the saturated intensities. With a small resonance detuning, similar mode frequency and gain behaviours are retained, albeit with only one mode now having the lowest saturated gain in the strong coupling region (Fig. 2c).

In the matched resonance case, provided the unsaturated gain g_1 is initially set slightly above the loss γ_2 in the receiver resonator, the power transfer efficiency at steady state is given by:

$$\eta = \frac{2\gamma_1 |a_2|^2}{2\gamma_{10}|a_1|^2 + 2\gamma_2 |a_2|^2} = \begin{cases} \dfrac{\gamma_1}{\gamma_2} \dfrac{1}{1 + \frac{\gamma_{10}\gamma_2}{\kappa^2}}, & \kappa < \gamma_2 \\[2ex] \dfrac{\gamma_1}{\gamma_2} \dfrac{1}{1 + \frac{\gamma_{10}}{\gamma_2}}, & \kappa \geq \gamma_2 \end{cases} \tag{5}$$

In the strong coupling region, the transfer efficiency is independent of κ and approaches unity in the limit $\gamma_{10}, \gamma_{20} \ll \gamma_1$. (Resonance detuning degrades the efficiency but the effect is small for a detuning within $|\omega_2 - \omega_1| < \gamma_2/2$, as shown in Extended Data Fig. 3.) Hence the efficiency is robust against fluctuation of distance or orientation of the resonators, both having the effect of changing κ. The efficiency in equation (5) matches the optimal efficiency for the conventional wireless transfer scheme based on two resonators and assuming frequency-tuning for each value of κ (Methods). Here, however, there is no need for any tuning. The nonlinear gain saturation guarantees the PT symmetry of the steady state in the strong coupling region and hence automatically guarantees the operating frequency that is optimal for wireless power transfer.

We demonstrate the theory presented above in a radio-wave frequency circuits. Previously, radio-frequency circuits have been used to demonstrate the physics of PT symmetry[29]. Our work differs in that we aim to demonstrate a robust wireless power transfer scheme. The gain element consists of a voltage amplifier A and a feedback resistor R_1 as shown on the source side of the full circuit model in Fig. 3a. Such a gain element provides a negative resistance. With a voltage gain of $A > 1$, the amplifier, together with the feedback resistor of resistance R_1, functions as a resistor with a resistance of $-R_1/(A - 1)$. This negative resistor feeds power to the source resonator, which is then coupled through magnetic induction to power the load (denoted by R_2) on the receiver resonator. Saturation arises naturally with our design from the amplifier's supply limit. To ensure that the circuit is saturated, we set the unsaturated gain rate slightly higher than the overall loss rate (by choosing a specific value of R_1), although the circuit operates similarly for other choices of R_1 that lead to higher values of unsaturated gain (Extended Data Fig. 4).

We perform Simulation Program with Integrated Circuit Emphasis (SPICE) time-domain circuit simulations using a piecewise saturation model for the amplifier. The mutual inductance values M used in the simulation are calculated based on two identical coils 58 cm in diameter
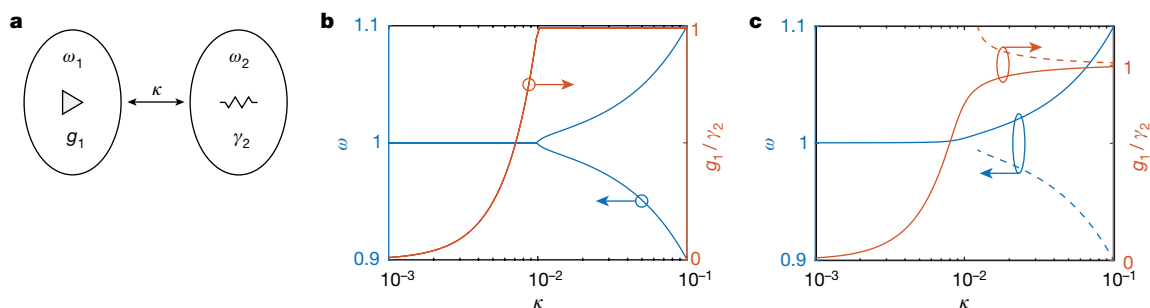
Figure 2 | Theory of operation. a, Coupled-mode theory model of a pair of coupled gain–loss resonators. Triangle indicates gain; resistor symbol indicates loss. **b, c,** Steady-state mode frequencies and their saturated gain rates as a function of coupling rate. The mode frequencies are obtained by solving equation (3) for a loss rate $\gamma_2 = 0.01$ and the gain rates from equation (4). When computed at matched resonance (**b**), $\omega_1 = \omega_2 = 1$, we can recover the solutions to the exact PT-symmetric phase in the strong coupling region ($\kappa \geq \gamma_2$) with balanced gain and loss ($g_1 = \gamma_2$) and mode frequency splitting of $2\sqrt{\kappa^2 - \gamma_2^2}$. In the weak coupling region ($\kappa < \gamma_2$), gain saturation reduces the steady-state gain ($g < \gamma_2$), and the steady state has a frequency of ω_1. Similar mode frequency behaviour survives with a small detuning (**c**): $\omega_1 = 1$, $\omega_2 = 0.999$; here the lower-frequency branch in the strong coupling requires a higher gain rate (dashed lines). In all these cases the steady-state frequencies are real.

spaced 20–120 cm apart (Methods and Extended Data Fig. 5). All other circuit parameters remain unchanged as the separation distance varies. The resonators' voltage ratio, frequency and phase are extracted from the simulated waveforms and shown in Fig. 3c–e (dashed lines). We repeat the simulations with the receiver's capacitance C_2 tuned up by 1 pF and R_1 lowered by 2 Ω to obtain the higher-frequency branch (magenta dashed lines). The results of the circuit simulation are generally in good agreement with the corresponding results obtained using coupled-mode theory (black lines). Therefore, such a circuit can indeed be used to demonstrate robust power transfer as predicted from the coupled mode theory.

On the basis of the circuit simulation we constructed a prototype as shown in Fig. 3b. Each of the two resonant coils is tuned to have a resonant frequency of 2.50 MHz. The coils have a measured intrinsic quality factor[4] of $Q = 300$. The receiver resonator was arranged on a wooden rod and able to slide coaxially towards or away from the source with the separation distance ranging from 20–120 cm. An operational amplifier, configured as a non-inverting amplifier with designed direct-current gain of 1.01, together with an adjustable resistor with resistance $R_1 \approx 40$ Ω, functions as a negative resistance element.

Figure 3c–e shows the ratio of voltage of the two resonators, the steady-state frequency, and the relative phase of the voltage of the two resonators, respectively. In all these results there is a good agreement between measurements and simulation. In particular, the efficiency, as measured by the voltage ratio (a proxy for $|a_2/a_1|^2$ in equation (5)), remains near unity as the distance between the source and the receiver
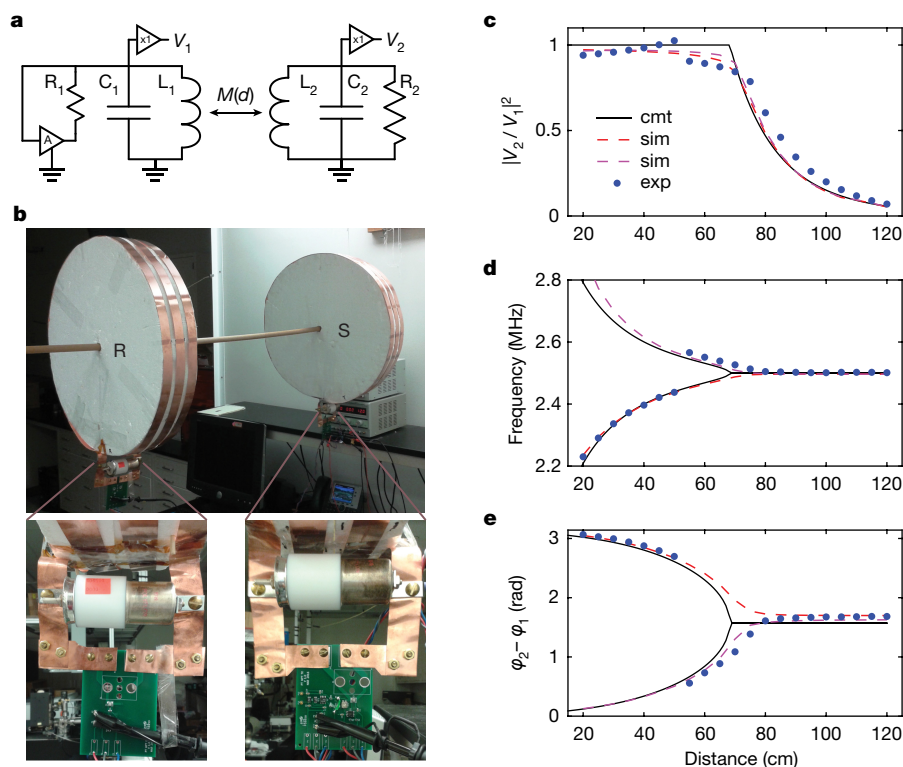
Figure 3 | Experimental verification of PT-symmetry-based wireless power transfer. a, Circuit theory model for PT-symmetric wireless power transfer, showing inductor (L), capacitor (C), resistor (R) and amplifier (A); the triangle marked '×1' is a voltage buffer. **b,** Photo of our experiment. S is the source resonator; R is the receiver. **c–e,** Coupled-mode theory (cmt), circuit simulation (sim) and experimental (exp) results showing voltage ratio (**c**), frequency (**d**) and phase (**e**). The two sets of simulations (red and magenta) use slightly different C_2 and R_1 values to make the frequency bifurcation visible. The parameters for the circuit simulations are provided in Extended Data Table 1.

resonators varies from 20 cm to approximately 70 cm, without the need for any tuning of the circuit. In the measurement, there is a transition of the steady-state frequency between the two frequency branches at a distance near 50 cm. Such a transition does not affect the transfer efficiency, and can arise from small detuning of the resonators (such as the one in Fig. 2c) combined with frequency dependence of the gain and random fluctuation. As the power supply to the amplifier is capped, the abrupt nature of the amplifier's gain saturation maintains the source resonator voltage amplitude at 10.5 V with minimal variation across the separation. Consequently, the power delivered to the load ($\propto |V_2|^2$) follows closely the curve shown in Fig. 3c. We further demonstrate the robustness of the PT power transfer scheme by replacing the receiver's load with a light-emitting diode (LED) bulb. In contrast to a conventional scheme where the LED brightness is highly dependent on the separation distance, our scheme produces a brightness that remains constant as the receiver is moved away from the source until a separation distance of around 1 m is reached (Methods and Supplementary Videos 1 and 2).

Further improvement in transfer efficiency can be achieved by reducing the parasitic loss, which, in the current setup, is dominated by the extra circuitry required for measurements, resulting in an intrinsic (unloaded) quality factor of around 300. The overall system efficiency is the product of the amplifier efficiency and the transfer efficiency we measure in the experiments. We use an off-the-shelf general-purpose amplifier designed to work over a wide bandwidth from direct current to 10 MHz; such an amplifier is not optimized for power efficiency and has a relatively low efficiency of about 10%. Given that the operating frequency of our system stays within a narrow range, highly efficient (>90%) switch-mode amplifiers operating in the frequency range could be designed for a practical system[30]. Our work also provides an experimental demonstration of phase transition in a nonlinear PT system, and thus points to a new direction in the experimental study of PT physics.

In conclusion, we present a theoretical study of a nonlinear PT-symmetric system incorporating a nonlinear gain saturation element. We show that this system can be used to achieve robust wireless power transfer; in particular, the frequency bifurcation leads to high and constant transfer efficiency in the strong coupling region without the need for active tuning. Circuit simulation and measurement data from a circuit prototype support the theoretical predictions.

1. Zierhofer, C. M. & Hochmair, E. S. High-efficiency coupling-insensitive transcutaneous power and data transmission via an inductive link. *IEEE Trans. Biomed. Eng.* **37,** 716–722 (1990).
2. Troyk, P. R. & Schwan, M. A. Closed-loop class E transcutaneous power and data link for microimplants. *Med. Biol. Eng. Comput.* **39,** 589–599 (1992).
3. Kurs, A. *et al.* Wireless power transfer via strongly coupled magnetic resonances. *Science* **317,** 83–86 (2007).
4. Yu, X. *et al.* Wireless power transfer in the presence of metallic plates: experimental results. *AIP Adv.* **3,** 062102 (2013).
5. Heetderks, W. J. RF powering of millimeter- and submillimeter-sized neural prosthetic implants. *IEEE Trans. Biomed. Eng.* **35,** 323–327 (1988).
6. Villa, J. L., Sallán, J., Llombart, A. & Sanz, J. F. Design of a high frequency inductively coupled power transfer system for electric vehicle battery charge. *Appl. Energy* **86,** 355–363 (2009).
7. Huh, J., Lee, S. W., Lee, W. Y., Cho, G. H. & Rim, C. T. Narrow-width inductive power transfer system for online electrical vehicles. *IEEE Trans. Power Electron.* **26,** 3666–3679 (2011).
8. Ho, J. S. *et al.* Wireless power transfer to deep-tissue microimplants. *Proc. Natl Acad. Sci. USA* **111,** 7974–7979 (2014).
9. Brecher, A. & Arthur, D. *Review and Evaluation of Wireless Power Transfer (WPT) for Electric Transit Applications.* FTA Report No. 0060, https://www.transit.dot.gov/sites/fta.dot.gov/files/FTA_Report_No._0060.pdf (US Department of Transportation, Federal Transit Administration, 2014).
10. Li, S. & Mi, C. C. Wireless power transfer for electric vehicle applications. *IEEE J. Emerg. Select. Topics Power Electronics* **3,** 4–17 (2015).
11. Tesla, N. Apparatus for transmitting electrical energy. US patent 1,119,732 (1914).
12. Brown, W. C. The history of power transmission by radio waves. *IEEE Trans. Microw. Theory Tech.* **32,** 1230–1242 (1984).
13. Sample, A. P., Meyer, D. A. & Smith, J. R. Analysis, experimental results, and range adaptation of magnetically coupled resonators for wireless power transfer. *IEEE Trans. Ind. Electron.* **58,** 544–554 (2011).
14. Bender, C. M. & Boettcher, S. Real spectra in non-Hermitian Hamiltonians having PT-symmetry. *Phys. Rev. Lett.* **80,** 5243–5246 (1998).
15. Bender, C. M., Brody, D. C. & Jones, H. F. Complex extension of quantum mechanics. *Phys. Rev. Lett.* **89,** 270401 (2002).
16. Guo, A. *et al.* Observation of PT-symmetry breaking in complex optical potentials. *Phys. Rev. Lett.* **103,** 093902 (2009).
17. Rüter, C. E. *et al.* Observation of parity–time symmetry in optics. *Nat. Phys.* **6,** 192–195 (2010).
18. Makris, K. G., El-Ganainy, R., Christodoulides, D. N. & Musslimani, Z. H. Beam dynamics in PT symmetric optical lattices. *Phys. Rev. Lett.* **100,** 103904 (2008).
19. Lin, Z. *et al.* Unidirectional invisibility induced by PT-symmetric periodic structures. *Phys. Rev. Lett.* **106,** 213901 (2011).
20. Peng, B. *et al.* Parity–time-symmetric whispering-gallery microcavities. *Nat. Phys.* **10,** 394 (2014).
21. Liertzer, M. *et al.* Pump-induced exceptional points in lasers. *Phys. Rev. Lett.* **108,** 173901 (2012).
22. Feng, L., Wong, Z. J., Ma, R.-M., Wang, Y. & Zhang, X. Single-mode laser by parity-time symmetry breaking. *Science* **346,** 972–975 (2014).
23. Hodaei, H., Miri, M.-A., Heinrich, M., Christodoulides, D. N. & Khajavikhan, M. Parity–time-symmetric microring lasers. *Science* **346,** 975 (2014).
24. Peng, B. *et al.* Loss-induced suppression and revival of lasing. *Science* **346,** 328–332 (2014).
25. Hassan, A. U., Hodaei, H., Miri, M. A., Khajavikhan, M. & Christodoulides, D. N. Nonlinear reversal of the PT-symmetric phase transition in a system of coupled semiconductor microring resonators. *Phys. Rev. A* **92,** 63807 (2015).
26. Ge, L. & El-Ganainy, R. Nonlinear modal interactions in parity-time (PT) symmetric lasers. *Sci. Rep.* **6,** 24889 (2016).
27. Haus, H. A. *Waves and Fields in Optoelectronics* 197–228 (Prentice Hall, 1984).
28. Siegman, A. E. *Lasers* 992–996 (University Science Books, 1986).
29. Schindler, J. *et al.* PT-symmetric electronics. *J. Phys. A* **45,** 444029 (2012).
30. Raab, F. H. *et al.* Power amplifiers and transmitters for RF and microwave. *IEEE Trans. Microw. Theory Tech.* **50,** 814–826 (2002).

Author Contributions S.A. performed the simulations and experiment. All authors contributed to formulating the analytical model, to analysing the data, and to writing the manuscript. S.F. initiated and supervised the project.

METHODS

Measurement setup. In each of the source and receiver resonators, the inductor element is made of three turns of 2.54 cm × 0.25 mm copper ribbon rolled around a 58-cm diameter foam core. The inductor element is in parallel with a 330-pF fixed capacitor on a circuit board and a standalone 5–85 pF tunable capacitor to allow tuning of their resonant frequencies to 2.50 MHz. A wooden rod maintains their coaxial alignment while allowing the receiver resonator to slide in and out of the source resonator. On the source's circuit board, the amplifier denoted A in Fig. 3a consists of an LM6171 high-speed operational amplifier configured as a non-inverting amplifier with $R_f = 510\,\Omega$ and $R_g = 5.1\,k\Omega$. The gain rate is trimmed to an appropriate value by an adjustable feedback resistor of resistance R_1, which is set to around $40\,\Omega$. This gain circuit runs on a $\pm 12\,V$ power supply. The receiver's circuit board hosts a resistor R2 with load $R_2 = 5.6\,k\Omega$. In addition, each resonator has a voltage follower, which run on a separate $\pm 15\,V$ power supply, buffering the resonators' voltages to an oscilloscope to allow measurements of the amplitudes and the phases of the voltage oscillation without noticeably interfering with the resonances. For simulations, we performed time-domain SPICE circuit simulations and analysed the waveforms for voltage ratio, frequency, and phases using the circuit parameters extracted from the experimental setup. We started each simulation with a small initial voltage ($1\,\mu V$) on the source resonator to kick start oscillations and waited until steady state was reached before recording the relevant waveforms. The amplifier saturation is modelled by limiting the output voltage of the amplifier. Extended Data Table 1 contains the circuit parameters used.

Stability analysis. In addition to the experimental demonstration, we support our claim that the steady state solution requiring the lowest gain that emerges from our nonlinear system dynamics is stable with the following stability analysis calculation[31,32]. Starting from the coupled-mode equation of the system:

$$\frac{d}{dt}\begin{bmatrix} a_1 \\ a_2 \end{bmatrix} = \begin{bmatrix} i\omega_1 + g_1(|a_1|) & -i\kappa \\ -i\kappa & i\omega_2 - \gamma_2 \end{bmatrix}\begin{bmatrix} a_1 \\ a_2 \end{bmatrix} \qquad (6)$$

where g_1 is a function of the magnitude $|a_1|$, we let $\tilde{a}_{1,2}$ denote the complex amplitudes of a steady state with the lowest gain at frequency ω. As shown in the main text, ω and $\tilde{a}_1$ satisfy:

$$(\omega - \omega_1)(\omega - \omega_2)^2 + \gamma_2^2(\omega - \omega_1) - \kappa^2(\omega - \omega_2) = 0$$

and

$$g_1(|\tilde{a}_1|) = \gamma_2 \frac{\omega - \omega_1}{\omega - \omega_2}$$

We apply perturbations $\rho_{1,2} \propto e^{\lambda t}$ around the steady-state solution $\tilde{a}_{1,2}e^{i\omega t}$, where λ is referred to as the Lyapunov exponent. In a frame rotating at ω, equation (6) gives the following equations for the perturbations:

$$\frac{d\rho_1}{dt} = A\rho_1 + B\rho_1^* + C\rho_2$$

and

$$\frac{d\rho_2}{dt} = C\rho_1 + D\rho_2$$

where $A = i(\omega_1 - \omega) - \gamma_2 + g_1(\tilde{a}_1) + \left.\frac{dg_1}{d|a_1|^2}\right|_{\tilde{a}_1}|\tilde{a}_1|^2$, $B = \frac{dg_1}{d|a_1|^2}\tilde{a}_1^2$, $C = -i\kappa$, and $D = i(\omega_2 - \omega) - \gamma_2$. We assume the gain has the form $g_1(|a_1|) = 2(\gamma_2 + \gamma_{10})/(1 + |a_1|^2) - \gamma_{10}$; however, the results generalize to any unsaturated gain level and saturation dependence. For a stable steady state, all the perturbations are decaying, $Re[\lambda] < 0$, except for one with $\lambda = 0$, which arises from the undetermined global phase[31].

Extended Data Fig. 1 shows that the steady state in the nonlinear PT wireless power transfer is stable across all range of separation distance and resonators' detuning. The marginal stability observed at the PT transition point in Extended Data Fig. 1a is due to the coalescence of the eigenmodes and is manifested in the actual power transfer system as a bifurcation point that has no effect on the transfer efficiency. The marginal stability disappears with resonator detuning (Extended Data Fig. 1b).

Transient response. Having a short transient response that settles quickly into a steady state relative to the speed of the receiver is critical in a robust dynamic wireless power transfer where the receiver might be moving. The nonlinear PT wireless power transfer system settles into its steady state much more rapidly than the timescale associated with mechanical motions, such that it is extremely difficult to observe any transient response with continuous movement of the

receiver in our measurements experimentally. To make the transient response visible, we induce sudden separation distance variations in the form of step functions in the time-domain simulations of equation (6), using parameters extracted from our experiment setup. The results shown in Extended Data Fig. 2 reveal that the system reaches steady state within microseconds. As shown in Extended Data Fig. 2a, the worst-case transient response occurs when the separation distance switches between the weak and strong coupling regions, passing through the PT phase transition point where bifurcation takes place. Nevertheless, the steady state is re-established within $50\,\mu s$ after the transient response dies away. For movements within the same region, the transient decay time is much shorter. Extended Data Fig. 2b shows transient response decays within $20\,\mu s$ in the event of sudden switching within the strong coupling region between the separation distances of 65 cm and 55 cm. The ultra-short transient time our proposed scheme offers makes it a viable option for use in dynamic wireless power transfer, including dynamic charging of vehicles travelling at motorway speed.

Efficiency of a conventional wireless power transfer scheme. The conventional wireless power transfer setup as shown in Fig. 1a can be described with a two-port power transfer model as shown in Extended Data Fig. 6. The coupled-mode equations in the model are as follows[4]:

$$s_{1-}(t) = -s_{1+}(t) + \sqrt{2\gamma_1}\,a_1(t)$$

$$\dot{a}_1(t) = (i\omega_0 - \gamma_{10} - \gamma_1)a_1(t) - i\kappa a_2(t) + \sqrt{2\gamma_1}\,s_{1+}(t)$$

$$\dot{a}_2(t) = (i\omega_0 - \gamma_{20} - \gamma_2)a_2(t) - i\kappa a_1(t)$$

and

$$s_{2-}(t) = \sqrt{2\gamma_2}\,a_2(t)$$

where $\gamma_{1(2)}$ are the loss rates arising from coupling between the source (receiver) and input (output) port, and $\gamma_{10(20)}$ are the intrinsic loss rates of the source (receiver) resonator. The waves s_{1+}, s_{1-} and s_{2-} are the input, reflected and output wave amplitudes, respectively, and $s_{2+} = 0$ because no power enters from the output port. For simplicity, we consider a symmetric case ($\gamma_1 = \gamma_2 = \gamma$ and $\gamma_{10} = \gamma_{20} = \gamma_0$). For an input harmonic wave at frequency ω, the transfer efficiency is:

$$\eta = \left|\frac{s_{2-}}{s_{1+}}\right|^2 = \left|\frac{\kappa\sqrt{2\gamma_1}\sqrt{2\gamma_2}}{\kappa^2 + [i(\omega - \omega_0) + \gamma_1 + \gamma_{10}][i(\omega - \omega_0) + \gamma_2 + \gamma_{20}]}\right|^2$$

which, for the symmetric case ($\gamma_1 = \gamma_2 = \gamma$ and $\gamma_{10} = \gamma_{20} = \gamma_0$), becomes:

$$\eta = \left|\frac{2\kappa\gamma}{\kappa^2 + (i\Delta\omega + \bar{\gamma})^2}\right|^2 \qquad (7)$$

where $\Delta\omega = \omega - \omega_0$ and $\bar{\gamma} = \gamma + \gamma_0$. To maximize η in equation (7) given a fixed γ_0, one must tune the input/output coupling $\gamma = \sqrt{\kappa^2 + \gamma_0^2}$ by adjusting the orientation of the input (output) coil relative to the source (receiver) resonator to avoid mode splitting and operate the system at its resonant frequency ($\omega = \omega_0$) as done in ref. 3. However, in a dynamic wireless power transfer scenario, tuning the coil-to-resonator coupling γ on the fly may not be practical. When a fixed coil-to-resonator coupling γ becomes an additional constraint, optimal efficiency is then obtained by frequency tuning[13,33], which adjusts the feeding frequency in response to the changing source–receiver coupling according to:

$$\omega = \begin{cases} \omega_0, & \kappa \leq \bar{\gamma} \\ \omega_0 \pm \sqrt{\kappa^2 - \bar{\gamma}^2}, & \kappa > \bar{\gamma} \end{cases}$$

resulting in high, constant transfer efficiency throughout the strong coupling region. Having such a frequency tuning results in a considerable improvement compared to a system without frequency tuning ($\omega = \omega_0$ for all values of κ) where the efficiency suffers when the receiver gets too close to the source. Figure 1c shows the efficiency comparison between the conventional scheme (with and without frequency tuning) and the PT-symmetric scheme for the following parameters: $\omega_0 = 1$, $\gamma_0 = 5 \times 10^{-4}$ and $\gamma = 0.0125$ for the conventional scheme and $\omega_{1,2} = 1$, $\gamma_{10,20} = 5 \times 10^{-4}$ and $\gamma_1 = 0.0125$ for the PT-symmetric scheme. The difference in the transfer efficiency between the conventional scheme with frequency tuning and the PT-symmetric scheme arises from the presence of reflection in the conventional scheme.

Coupling rate versus separation distance. Magnetic field coupling is preferred in wireless power transfer applications since most everyday materials do not

interact strongly with magnetic fields. The design of the coils as well as the environment the fields occupy strongly affects how the coupling rate changes with the coils' separation distance and orientation. Techniques such as magnetic field shaping to enhance the coupling strength[34] have the potential to improve transfer range and efficiency further. In this work, we examine power transfer and PT symmetry between two copper coils spaced coaxially apart at various distances. In the quasi-static limit, the coupling rate between two identical coils is related to the mutual inductance by $2\kappa/\omega_0 = M/L$ where M (L) is the mutual (self) inductance and can be calculated from:

$$M = \frac{\mu_0 r^2}{2l} \int_0^{1-\frac{w}{2r}} \theta I_\mathrm{B}\left(\theta, \frac{d}{a}\right) d\theta \qquad (8)$$

$$L = \frac{\mu_0 r^2}{2l} \int_0^{1-\frac{w}{2r}} \theta I_\mathrm{B}(\theta, 0) d\theta \qquad (9)$$

$$I_\mathrm{B} = \int_0^{2\pi} \int_{-\frac{l}{2r}}^{\frac{l}{2r}} \frac{1 - \theta\cos\phi}{[(\Omega - \xi)^2 + 1 + \theta^2 - 2\theta\cos\phi]^{\frac{3}{2}}} d\xi d\phi \qquad (10)$$

where the relevant dimensions are given in Extended Data Fig. 5a. By measuring the frequency splitting in the transmission spectrum of the two tuned resonant coils at various distances, we can experimentally find the coupling rate κ using the relation $\kappa = \sqrt{\gamma_0^2 + (\Delta\omega/2)^2}$ where γ_0 is the intrinsic loss rate and $\Delta\omega$ is the frequency splitting. Extended Data Fig. 5b shows an excellent agreement between the calculated and experimental values. Note that the coupling rate reduces by one order of magnitude as the distance increases from 20 cm to 60 cm. Thus, any scheme that relies on coupling-dependent parameter tuning to achieve high efficiency would not be viable in the dynamic power transfer scenario where the receiver continuously moves around the source, for example, power delivery to a moving vehicle.

Wireless power transfer scheme visualization. As a visualization of the wireless power transfer process, we replace the receiver's circuit board with another one containing just a 330 pF high-Q capacitor connected to a full-wave rectifier and a 1 kΩ resistor in series with a 5.5-Cd white LED as a load. Another adjustable capacitor is added to the receiver coil to increase its tuning range to match the source's resonance frequency (now at 2.47 MHz). With this configuration, the LED starts to emit faintly when the amplitude to the rectifier circuit reaches 3.5 V and becomes brightly lit when the voltage increases to 4.0 V. The power supply to the source is reduced to ±5.5 V so that the saturated amplitude in the source resonator is around 4.0 V, a power level that lights up the LED brightly. As a result of this arrangement, the PT phase transition from the unbroken to the broken phases coincides with the LED on/off states. As the receiver is moved in and out of the source, the brightness level on the receiver remains constant for a wide range of separation distance of up to 1 m (see Supplementary Video 1) as a manifestation of the robust power transfer of the PT-symmetric scheme. In contrast, we repeat the experiment with a conventional wireless power transfer setup where the gain circuit is removed; instead, the power is fed into the source resonator via a coil (44 cm in diameter, placed next to the source resonator) connected to a function generator producing a sinusoidal wave with voltage amplitude 0.5 V at the circuit resonance (2.47 MHz). As shown in Supplementary Video 2, the LED brightness varies as a function of the separation distance, with the brightness reaching its maximum around 60 cm and dimming once the receiver moves closer or further away.

Data availability. The data supporting the findings of this study are available within the paper. Source Data for Figs 1–3 are available in the online version of the paper.

31. Cerjan, A. & Stone, A. D. Steady-state *ab initio* theory of lasers with injected signals. *Phys. Rev. A* **90,** 013840 (2014).
32. Zhou, X. & Chong, Y. D. PT symmetry breaking and nonlinear optical isolation in coupled microcavities. *Opt. Express* **24,** 6916 (2016).
33. Kim, N. Y., Kim, K. Y., Choi, J. & Kim, C.-W. Adaptive frequency with power-level tracking system for efficient magnetic resonance wireless power transfer. *Electron. Lett.* **48,** 452 (2012).
34. Shin, J. *et al.* Design and implementation of shaped magnetic-resonance-based wireless power transfer system for roadway-powered moving electric vehicles. *IEEE Trans. Ind. Electron.* **61,** 1179–1192 (2014).
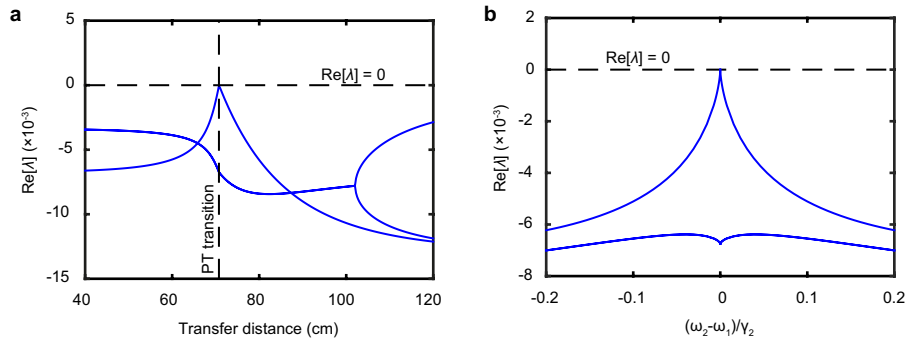
Extended Data Figure 1 | Stability analysis for the steady-state solution with the lowest gain. a, Lyapunov exponents are of the decaying type, showing that the steady-state solution with the lowest gain is stable for all transfer distances. At the PT transition point, the eigenmodes coalesce, resulting in marginal stability along with frequency bifurcation, which has no effect on the transfer efficiency. The coupling rates are extracted from our experimental setup and $\omega_1 = \omega_2 = 1$, $\gamma_{10} = 5 \times 10^{-4}$, $\gamma_2 = 0.013$. **b**, Lyapunov exponents versus resonator detuning at the PT transition point. The marginal stability disappears with non-zero resonator detuning.
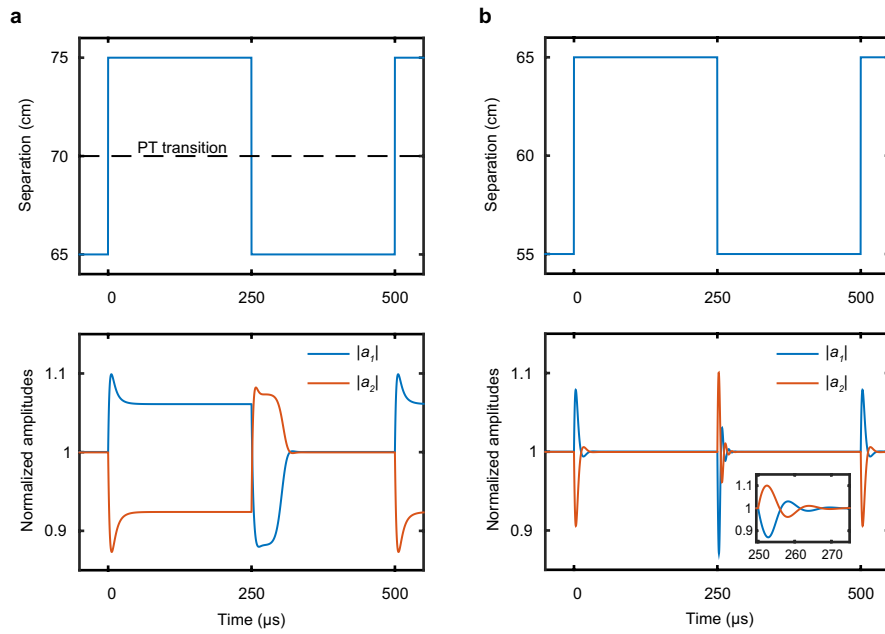
Extended Data Figure 2 | Simulated transient response to sudden movements of the receiver. Effect of sudden changes in the separation distance (top panels) on the mode amplitudes $a_{1,2}$ (bottom panels). **a**, For a sudden shift in the separation distance between 75 cm and 65 cm, the nonlinear PT power transfer system settles into its steady state within $50\,\mu s$. The move across the PT phase transition point represents the worst case for the transient decay time. **b**, The transient response becomes shorter away from the PT phase transition. Here, a sudden shift in distance from 65 cm to 55 cm results in less than $25\,\mu s$ of transient decay time. The

inset (same axes as the main panel) shows a magnified transient response at around $250\,\mu s$. These transient response times are much shorter than the typical timescale of mechanical motions, demonstrating the viability of our proposed system for dynamic wireless power transfer. The simulations are performed by solving equation (6) in the time domain using the coupling rates extracted from the experimental setup and other pertinent parameters as follows: $\omega_1 = \omega_2 = 2\pi \times 2.50\,\mathrm{MHz}$, $\gamma_{10} = 2\pi \times 1.25\,\mathrm{kHz}$, $\gamma_2 = 2\pi \times 32.5\,\mathrm{kHz}$, and $g_1(|a_1|) = 2(\gamma_{10} + \gamma_2)/(1 + |a_1|^8)$.
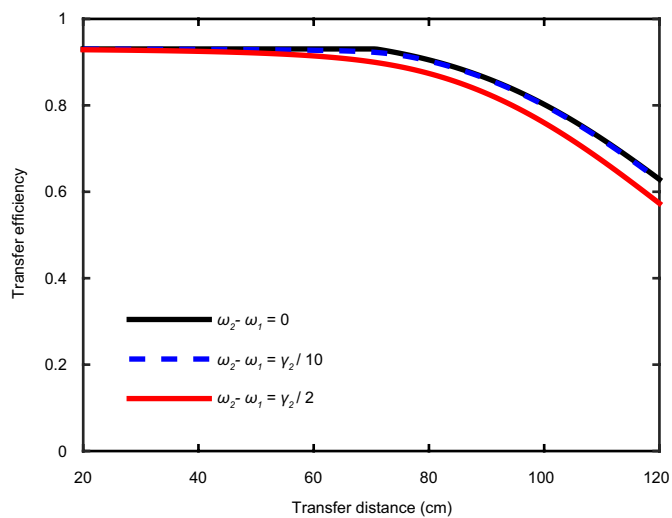
Extended Data Figure 3 | Tolerance to resonator detuning. The transfer efficiency (equation (5)) is plotted as the receiver's resonant frequency ω_2 is detuned away from that of the source ω_1. The range of acceptable detuning is limited to around the receiver's linewidth γ_2. The same limit also applies to other forms of resonant power transfer. The coupling rates are extracted from our experimental setup, $\omega_1 = 1$, $\gamma_{10} = \gamma_{20} = 5 \times 10^{-4}$ and $\gamma_2 = 0.013$.
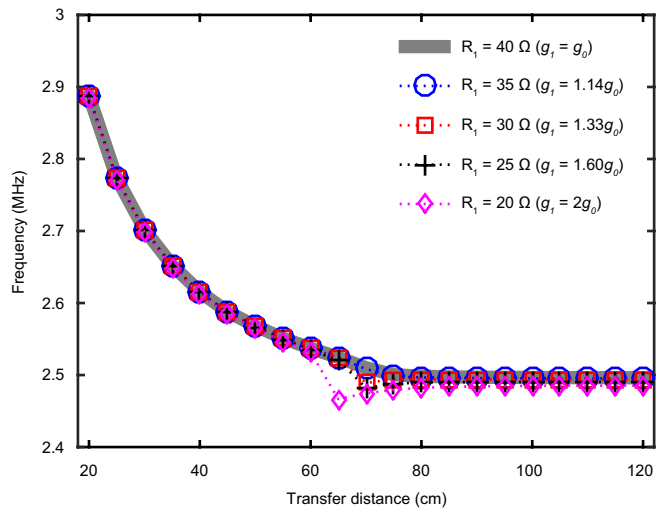
Extended Data Figure 4 | Steady-state frequency as a function of unsaturated gain value. The unsaturated gain rate is adjusted via resistor R_1 in the circuit simulation with other circuit parameters fixed (Extended Data Table 1). The mode frequency remains largely unchanged as the source resonator's unsaturated gain g_1 is increased from near its required minimum value, g_0, to $2g_0$. The only mode switching observed occurs at $g_1 = 2g_0$, near the transfer distance of 70 cm, where the system crosses the PT transition point. Since both frequency branches offer identical performance when the source's and receiver's resonances are tuned, the effect of mode switching to the other branch on the system performance here is minimal.

a

b
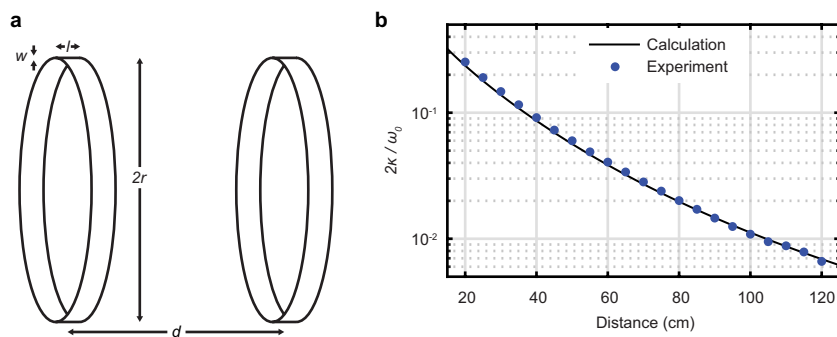
Extended Data Figure 5 | Coupling rate as a function of separation distance. a, Coil dimensions for the coupling rate calculation (equations (8)–(10)) are as follows: $w = 0.25$ mm, $l = 2.54$ cm and $2r = 58$ cm. **b**, Comparison of the calculated and experimental values of the coupling rate as a function of the separation between the two coaxially aligned coils.
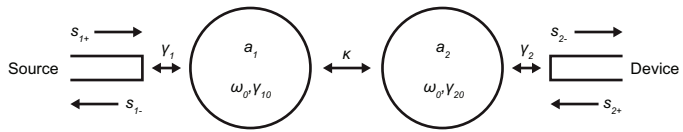
Extended Data Figure 6 | Detailed coupled-mode model for a conventional wireless power transfer scheme.

Extended Data Table 1 | Circuit parameters used in the simulations

Parameter	Source	Receiver
Inductance ($L_{1,2}$)	9.13 μH	8.92 μH
Capacitance ($C_{1,2}$)	444 pF	454 pF (455 pF)
Resonant frequency ($\omega_0/2\pi$)	2.50 MHz	2.50 MHz
Resonator intrinsic factor (Q_0)	305	306
Voltage amplification (A)	1.01 V/V	
Gain resistance (R_1)	42 Ω (40 Ω)	
Load resistance (R_2)	5.6 kΩ	
Mutual inductance ($M/(L_1L_2)^{1/2}$)	0.25 - 0.0066	

The numbers in parentheses are used to simulate the higher-frequency branch.